NANO LETTERS

Letter

pubs.acs.org/NanoLett

Optimization of Chiral Structures for Microscale Propulsion

Eric E. Keaveny,*[,†] Shawn W. Walker,[‡] and Michael J. Shelley[§]

[†]Department of Mathematics, Imperial College London, South Kensington Campus, London, SW7 2AZ, United Kingdom

[‡]Department of Mathematics and Center for Computation and Technology, Louisiana State University, Lockett Hall, Baton Rouge, Louisiana 70803-4918, United States

[§]Applied Mathematics Lab, Courant Institute, New York University, 251 Mercer Street, New York, New York, 10012, United States

Supporting Information

ABSTRACT: Recent advances in micro- and nanoscale fabrication techniques allow for the construction of rigid, helically shaped microswimmers that can be actuated using applied magnetic fields. These swimmers represent the first steps toward the development of microrobots for targeted drug delivery and minimally invasive surgical procedures. To assess the performance of these devices and improve on their design, we perform shape optimization computations to determine swimmer geometries that maximize speed in the direction of a given applied magnetic torque. We directly assess aspects of swimmer shapes that have been developed in previous experimental studies, including helical propellers with elongated cross sections and attached payloads. From these optimizations, we identify key improvements to existing designs that result in swimming speeds that are 70−470% of their original values.

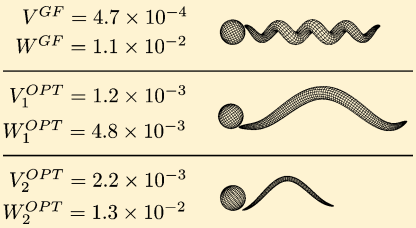

KEYWORDS: *Microswimmers, shape optimization, chiral, microfluidics, fluid-structure interaction, simulation*

Micro- and nanoscale magnetic structures have served as essential building blocks to a number of devices, including microfluidic pumps,[1] controlled and localized micromixers,[2,3] and high-throughput DNA size selectors.[4] One of the most novel and notable applications of these magnetic particles has been in the construction of micro- and nanoscale biomimetic swimmers.[5−13] These devices are powered by time-dependent magnetic fields and utilize locomotion strategies similar to those exhibited by swimming cells and microorganisms to move in an environment where viscosity dominates and inertial effects are negligible.[14,15] While often referred to as artificial swimmers, they are not true self-propelled bodies since they are driven by an applied magnetic torque. Two significant examples are the rigid, helical swimmers developed in Zhang et al.[8−10] and Ghosh and Fischer.[7] These swimmers have been shown to be highly controllable and able to follow complex swimming paths in three dimensions. These characteristics are particularly attractive for future biomedical applications as microrobots for highly targeted drug delivery and precise, minimally invasive surgical procedures.[16,17]

Key to the performance of these devices is their geometry. It is their helical shape that couples rotation and translation[18] and allows the torque generated by an applied rotating magnetic field to induce translation. While both the Zhang et al. and Ghosh and Fischer swimmers rely on this strategy for propulsion, there are distinct differences in their geometries that arise due to the different techniques used to synthesize them. The geometric differences lead to different hydrodynamic mobilities and couplings of the applied magnetic torque to the linear translation velocity. A natural question to ask is what swimmer geometries maximize this coupling. To help answer this question, we turn here to the computational techniques of shape optimization.[19,20] Optimization techniques have already been successful in elucidating aspects of microorganism locomotion, including the beat patterns of flagellated cells,[21−24] wave shapes in lubrication-layer propulsion and pumping,[25,26] and effective slip-velocities generated by ciliated organisms.[27] We show here that these methods are also powerful tools in establishing design principles for artificial microswimmers. An important aspect of our approach is the use of a boundary integral formulation[28,29] of the Stokes equations to accurately determine the swimming speed and how it varies with swimmer shape. This complete treatment of the hydrodynamics allows us to move beyond simple drag-based models and consider the effects of the finite thickness of the propeller as well as attached cargo, important geometric features of both the Zhang et al. and Ghosh and Fischer swimmers.

While the microswimmers in Zhang et al. and Ghosh and Fischer are constructed using very different techniques, they are both rigid bodies that contain magnetic material. The interaction between this material and an applied magnetic field results in a torque, $\boldsymbol{\tau}$, on the swimmers, allowing for actuation and direction by the applied field. If this field is spatially uniform, as it was in both experiments, the magnetic force on the swimmers will be zero, $\mathbf{F} = 0$. As a result, translational motion requires there be a coupling between the magnetic torque and the linear velocity. Given the small size of

Received: November 2, 2012
Revised: January 8, 2013

dx.doi.org/10.1021/nl3040477 | *Nano Lett.* XXXX, XXX, XXX−XXX

the swimmers, the Reynolds number[18] associated with their motion is Re ≈ 10^{-4}–10^{-3}, indicating that the effects of inertia are negligible. Accordingly, there will be a linear relationship,

$$\begin{bmatrix} \mathbf{U} \\ \mathbf{\Omega} \end{bmatrix} = \mathcal{M} \begin{bmatrix} \mathbf{F} \\ \boldsymbol{\tau} \end{bmatrix} \tag{1}$$

between the swimmer's linear velocity, **U**, and angular velocity, **Ω**, and the applied force **F** and torque $\boldsymbol{\tau}$. These equations, based on continuum fluid mechanics, can describe the average motion of nanoscale structures much smaller than the Ghosh and Fischer swimmer (for example, see Drazer et al.[30]). While the relationship (eq 1) is linear, the entries of the 6 × 6 mobility matrix, $\mathcal{M}$, depend nonlinearly on the geometry of the swimmer. The purpose of our study is to determine the swimmer geometries that maximize the matrix entries that couple the torque and linear velocity in a particular direction. Since the Reynolds number is much less than 1, this shape will not depend on the fluid viscosity. Also, due to the scale invariance of low Reynolds number hydrodynamics, the optimal shape will not depend on the overall size of the swimmer. Only the speed will be affected by swimmer size. This is important to note since the Ghosh and Fischer swimmer is an order of magnitude smaller than that Zhang et al. Finding the mobility matrix entries requires solution of the Stokes equations

$$\begin{aligned} -\nabla p + \eta \nabla^2 \mathbf{u} &= 0 \\ \nabla \cdot \mathbf{u} &= 0 \end{aligned} \tag{2}$$

for the pressure field, p, and fluid velocity **u**, when the total force on the swimmer is zero, the torque is $\boldsymbol{\tau}$, and $\mathbf{u} = \mathbf{U} + \mathbf{\Omega} \times \mathbf{x}$ on the surface of the swimmer. By taking $\boldsymbol{\tau} = \mathbf{e}_i$ for i = 1, 2, or 3 and solving for the corresponding components of **U** and **Ω**, the entries of the matrix $\mathcal{M}$ that couple linear velocity and applied torque can be found. Given the complexity of the swimmer geometries, this problem is solved most accurately and efficiently using a boundary integral formulation of Stokes flow. As described in the Supporting Information, we utilize a second-kind boundary integral equation for the tractions on a rigid body and determine numerical solutions using the second-order accurate trapezoidal rule for surface quadratures.[29] This formulation avoids the numerical ill-conditioning associated with the standard first-kind integral equation,[28] allowing us to determine the surface tractions to the high accuracy necessary for optimization.

A straightforward way of finding optimal shapes is to take a particular parametrization of the swimmer geometry and compute the mobility matrix entries for different values of the shape parameters, seeking those values that maximize a specified objective function. This simple approach is very useful for improving the speed of the Zhang et al. swimmer where we optimize over a single parameter that controls the orientation of the propeller's elongated cross-section.

A computational model of the Zhang et al. swimmer is depicted in the top image of Figure 1a (cf. Figure 1g of Zhang et al.[8]). The parametrization of this swimmer's surface is described in the Supporting Information, though to understand the results that follow, we mention two aspects of this parametrization. The first is that the centerline of the swimmer's propeller is given by the simple helix

$$\mathbf{X}_{\mathrm{hel}}(s) = b(\cos ks\hat{\mathbf{x}} + \sin ks\hat{\mathbf{y}}) + \alpha s\hat{\mathbf{z}} \tag{3}$$

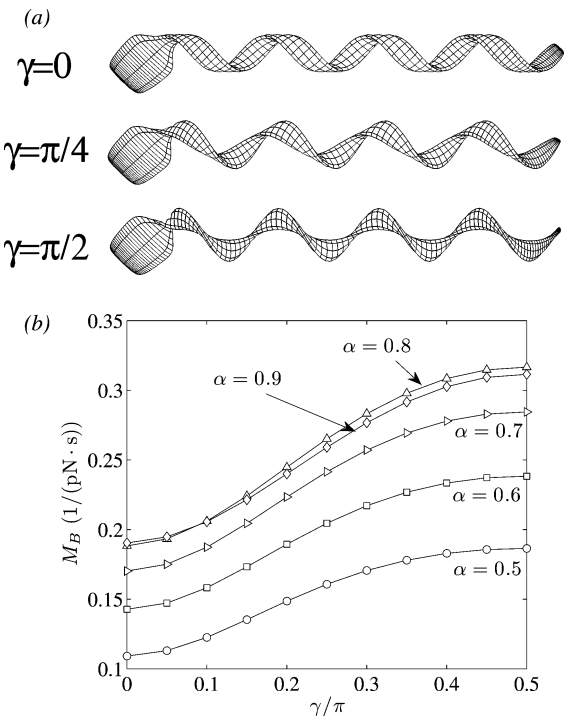

Figure 1. (a) Swimmer shapes with α = 0.7 and with the indicated values of the propeller cross-section orientation parameter γ. The Zhang et al.[8−10] swimmer geometry corresponds to γ = 0 (top image). (b) The rotation-translation coupling mobility matrix entry M_B as a function of γ for different values of the centerline slope parameter α.

with $\alpha^2 + b^2k^2 = 1$. The parameter b is the radius of the helix, while k and α determine its wavelength $\Lambda = 2\pi/k$ and pitch $\lambda = \alpha\Lambda$. The helical axis and the swimming direction are taken to be $\hat{\mathbf{z}}$. The second aspect of the parametrization is that the orientation of the propeller cross-section is controlled by a rotation angle, γ. Figure 1a shows the swimmer shapes for α = 0.7 and $k = 4\pi/L$ with γ = 0, $\pi/4$, and $\pi/2$. With γ = 0, we model the Zhang et al. swimmer, while for $\gamma = \pi/2$, the long axis of the propeller cross-section is turned to be perpendicular to the helical axis.

With this description of the swimmer's surface, we can solve the boundary integral equations and obtain the mobility matrix entries for the swimmer. We can validate these calculations by comparing with the experimental results of Zhang et al.[9] Given the swimmer's helical symmetry, the force and torque in the swimming direction $\hat{\mathbf{z}}$ can be approximated by $F_z = R_A U_z + R_B \Omega_z$ and $\tau_z = R_B U_z + R_D \Omega_z$ respectively, where U_z is the swimming speed, Ω_z is the rotational speed about $\hat{\mathbf{z}}$, and R_A, R_B, and R_D are resistance coefficients. Zhang et al.[9] performed a series of experiments to estimate the resistance coefficients and obtained $R_A^Z = 1.5 \times 10^{-7}$ N·s/m, $R_B^Z = 1.6 \times 10^{-14}$ N·s, and $R_D^Z = 2.3 \times 10^{-19}$ N·m·s. If we take the propeller length to be 49.7 μm and the viscosity to be $\eta = 10^{-3}$Pa·s as they were in these experiments, for the parameter values α = 0.7 and γ = 0 (Figure 1a, top image), our boundary integral calculations yield the resistance coefficients, $R_A^{BI} = 9.37 \times 10^{-8}$ N·s/m, $R_B^{BI} = 1.63 \times 10^{-14}$ N·s, and $R_D^{BI} = 1.01 \times 10^{-18}$ N·m·s. These values, especially R_B^{BI}, are comparable to the measured values, despite the slight differences in swimmer geometry and the hydrodynamic interactions with channel walls present in the experiments. The wall interactions will become significant when the distance (not provided in Zhang et al.[9]) from the

dx.doi.org/10.1021/nl3040477 | Nano Lett. XXXX, XXX, XXX–XXX

swimmer to the surface is comparable to the swimmer's length (see Spagnolie and Lauga[31]). Correspondence with the experimental value of R_B is particularly important since it is this resistance coefficient that governs the speed-torque coupling.

We now focus our attention on the mobility matrix entry M_B that determines the swimming speed when there is an applied torque about the swimming direction. It is given by $M_B = U_z/\tau_z$ when all other components of the applied force and torque are zero. Figure 1b shows how M_B varies with the parameter γ, for different values of α, while keeping both the size of the swimmer's head and the value of $k = 4\pi/L$ fixed. We find that the largest values of M_B occur when $\gamma = \pi/2$. This corresponds to the long axis of the propeller cross-section being perpendicular to the swimming direction, giving an Archimedean screw (see Figure 1a, bottom image). Depending on the value of α, we find that the Archimedean screw ($\gamma = \pi/2$) swimmer has a speed between 165% to 170% faster than that of the $\gamma = 0$ swimmer. These increases in speed are comparable to those found for helices without the attached head[29] but are much greater than the modest speed increases of 9% that were predicted using simple drag based models.[10] Overall, the highest value of $M_B = 0.32(\text{pN}\cdot\text{s})^{-1}$ was achieved when $\alpha = 0.8$ and $\gamma = \pi/2$. This value is 1.8 times that of our computed value for the Zhang et al. swimmer ($\alpha = 0.7$ and $\gamma = 0$). It is important to note that nearly all of this increase is due to the reorientation of the propeller cross-section.

We demonstrated that by varying a single parameter that controlled the orientation of the propeller cross-section the speed of the Zhang et al. swimmer could be increased to 170% of its original value. Identifying improvements to the Ghosh and Fischer swimmer requires more sophisticated techniques of shape optimization. Here, the optimization is performed over the shape of an elongated propeller of circular cross-section.

A computational model of the Ghosh and Fischer swimmer is shown in the top image of Figure 4 (cf. Figure 1B in Ghosh et al.[7]). We describe its propeller surface as

$$\mathbf{x}(s,\theta) = \mathbf{X}(s) + a_c(s)[\cos\theta\mathbf{n}_1(s) + \sin\theta\mathbf{n}_2(s)] \quad (4)$$

where arclength $s \in [-L,L]$ and angle $\theta \in [0,2\pi)$ are the coordinates, with $a_c(s) = a(1 - (s/L)^2)^{1/2}$ the cross-sectional radius, and $\boldsymbol{n}_1(s)$ and $\boldsymbol{n}_2(s)$ being two unit vectors orthogonal to $d\mathbf{X}(s)/ds$ and to each other. We solve the Stokes equations, eq 1, subject to the condition $\mathbf{u} = \mathbf{U} + \Omega_0(\hat{\mathbf{z}} \times \mathbf{x})$ on the swimmer surface with translational velocity $\mathbf{U}$ and rotational speed Ω_0. We also require that $\mathbf{F} = 0$ and that the torque has the form $\boldsymbol{\tau} = \tau_0\hat{\mathbf{z}} + \mathbf{T}$ given $\mathbf{T}\cdot\hat{\mathbf{z}} = 0$ and τ_0. The torque $\mathbf{T}$ ensures the axis of rotation is aligned with $\hat{\mathbf{z}}$. The unknowns are the translation velocity $\mathbf{U}$, the (scalar) rotation-rate Ω_0, and the two (x and y) components of the torque $\mathbf{T}$. This set of conditions is chosen to capture magnetic actuation where the swimmer is aligned and rotated by the applied magnetic field. Again, $\hat{\mathbf{z}}$ is the axis of alignment, rotation, and the swimming direction. The goal is to find the shape of $\mathbf{X}(s)$ that maximizes $U_z = \mathbf{U}\cdot\hat{\mathbf{z}}$ when the torque rotating the body, $\tau_0\hat{\mathbf{z}}$, is held fixed. To do so, we begin with an initial shape of $\mathbf{X}(s)$ and we use our boundary integral formulation to compute U_z and its *shape derivative*. The shape derivative quantifies how the swimming speed varies with perturbations in $\mathbf{X}(s)$ while maintaining the conditions on the applied force, torque, and angular velocity. With this information, we then use a steepest ascent method to find a subsequent swimmer shape that has a higher swimming speed while satisfying the constraints that s remain an arclength parametrization and that the total length $L_T = 2L$ and aspect ratio $\zeta = L/a$ remain constant. The process is iterated to generate a sequence of swimmer shapes with speeds that approach a locally maximum value. A more detailed description of our shape optimization can be found in the Supporting Information.

Using this shape optimization routine, we first consider the Ghosh and Fischer propeller in the absence of a payload and explore how the optimal shape of $\mathbf{X}$ depends on the aspect ratio of the propeller. Figure 2a shows the initial and final shapes from side and top views for three representative optimizations. The body aspect ratios $\zeta = 20$, 30, and 50 are indicated for each case. The changes in the propeller shape during each optimization can be seen in Supplementary Videos 1, 2, and 3. Figure 2b shows the x and y components of $\mathbf{X}(s)$ for the final swimmer shapes. Figure 3a shows the increase in speed over the course of each optimization. We find that even though the optimizations were initiated using complicated shapes, $\mathbf{X}(s)$ evolves into what closely resembles a simple helix. We find that as the aspect ratio of the body increases, the optimal shape has a greater number of helical turns. From Figure 2, we also see that the helical radius, the distance from the propeller centerline to the z-axis, decreases with increasing ζ. We do find, however, when normalized by the propeller cross-section radius a, these values become very similar. Though not shown, we also found that the z-component of each optimal centerline is well fit by the line $Z = \bar{\alpha}s$ with $\bar{\alpha} = 0.842$.

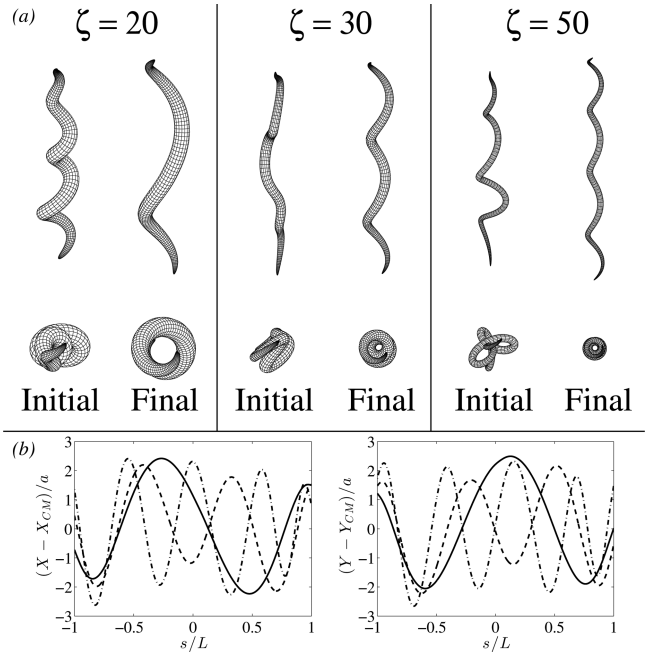

Figure 2. (a) Initial and optimized final shapes for bodies with aspect ratios 20, 30, and 50. (b) The x and y components of $\boldsymbol{X}(s)$ for the optimal shapes. The solid line corresponds to the case where $\zeta = 20$, the dashed line for $\zeta = 30$, and the dash-dotted line for $\zeta = 50$.

To better understand these observations, we have computed the speed for propellers with perfectly helical centerlines (see eq 3), varying either α and k or α and b. We performed these calculations for values of ζ between 20 and 100. The values of the speed are shown in Figure 3b for the extreme cases of $\zeta = 20$ and 100. We find that, for each case and regardless of the aspect ratio, the speed attains its peak value when $\alpha \approx 0.84$ and

dx.doi.org/10.1021/nl3040477 | Nano Lett. XXXX, XXX, XXX−XXX

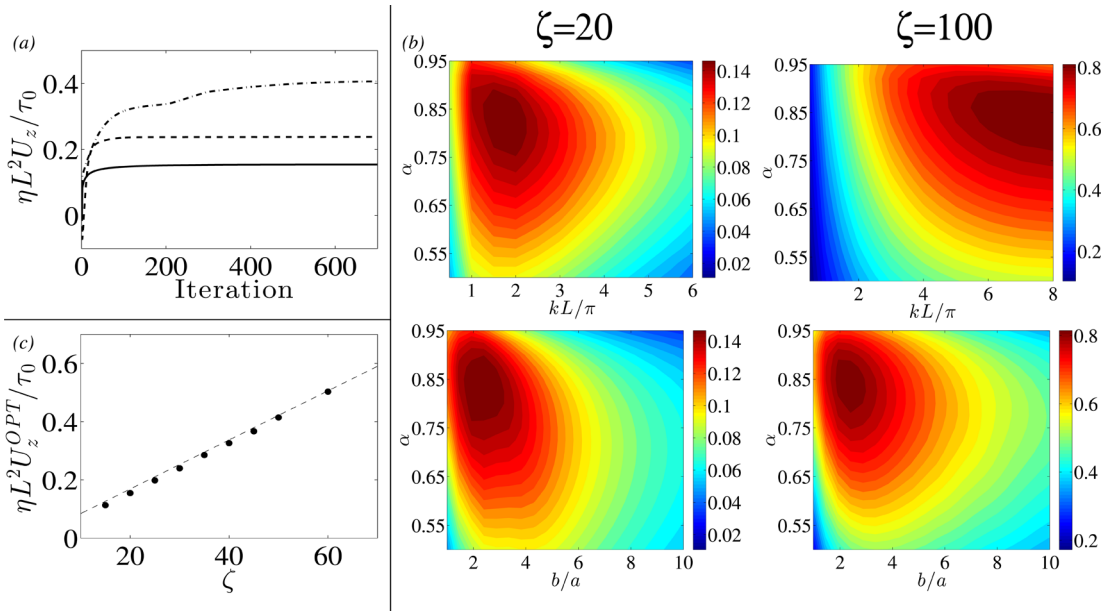

Figure 3. (a) The dimensionless speed over the course of the optimization for bodies with aspect ratio $\zeta = 20$ (solid line), $\zeta = 30$ (dashed line), and $\zeta = 50$ (dash-dotted line). (b) Contour plots showing the $\eta L^2 U_z/\tau_0$ for simple helices with aspect ratios $\zeta = 20$ and 100. In the top row, the contours are shown as a function of α and kL/π, while the bottom row shows the contours as a function of α and b/a. (c) The dimensionless speed of the optimal shapes as a function of the aspect ratio, ζ (black circles). The dashed line indicates the speeds of the optimal helices ($\alpha = 0.84$ and $b/a = 2.2$) as given by resistive force theory, eq 5.

$b/a \approx 2.2$. These values of α and b together with the inextensibility condition, $b^2k^2 + \alpha^2 = 1$, indicate that the number of turns should increase as the aspect ratio increases. This is indeed what was observed in the centerline optimizations. We tested the optimality of a helical centerline with $\alpha = 0.84$ and $b/a = 2.2$ by using it as the initial shape for $\boldsymbol{X}(s)$ in the centerline optimization. We found that the final shape is only slightly different from the initial helix, and that the speed is increased by at most 2%, demonstrating that helical centerlines with $\alpha = 0.84$ and $b/a = 2.2$ do indeed deliver nearly optimal performance.

Figure 3c shows the speed of the optimal propeller as a function of ζ. We find that it grows linearly with ζ and goes to infinity as the propeller becomes thinner and thinner. To understand this dependence, we again turn to a helical centerline and utilize a resistive force model to obtain a relationship between the swimming speed and the applied torque. In this model, the force per unit length, $\mathbf{q}$, is given by $\mathbf{q}(s) = (C_{\parallel}\mathbf{tt} + C_{\perp}(\mathbf{I} - \mathbf{tt}))v$, where v is the velocity of the centerline and $C_{\parallel}$ and $C_{\perp}$ are the drag coefficients for motions parallel and perpendicular to the centerline, respectively. Using Lighthill's formula[32] for these drag coefficients, $C_{\parallel} = 2\pi\eta/\log(2Q/a)$ and $C_{\perp} = 4\pi\eta/(\log(2Q/a) + 0.5)$ where $Q = 0.18\pi/k$, and taking the velocity of the centerline to be $\mathbf{v} = \mathbf{U} + \Omega_0\hat{\mathbf{z}} \times \mathbf{X}$, we can determine the following relationship between an applied torque in the z-direction and the swimming speed when the total force is zero:

$$U_z/\tau_z = \alpha k(C_{\perp} - C_{\parallel})/(2LC_{\perp}C_{\parallel}) \quad (5)$$

This is shown as the dashed line in Figure 3c for the helix with $\alpha = 0.84$ and $b/a = 2.2$. We see that this model provides an accurate estimate of the optimal speeds. Also, with these values of α, b/a, and $k = 0.25\zeta/L$, we see that U_z grows linearly with ζ. It is interesting to note that, even though this drag based model does accurately characterize the speed of the optimal shape, it cannot be used to predict the shape itself. Resistive force theory is a local approximation of the hydrodynamic force and does not set a length scale in the optimization problem. As a result, resistive force theory will always predict a body with an infinite number of helical waves as the optimal shape.[22] In Figure 3c, we see this corresponds to the case where $\zeta \to \infty$ and the swimming speed diverges.

Important to the utility of microswimmers will be the ability to pick-up and deliver a cargo to a specific location. It is essential to biomedical applications, especially targeted drug delivery. Swimmers incorporating this functionality have been explored experimentally by Tottori et al.[33] and have a geometry similar to the Ghosh and Fischer[7] swimmer. The presence of the cargo alters the overall swimmer geometry and so modifies the mobility matrix entries (i.e., the coupling of torque to linear velocity). We show here that these modifications dramatically alter the optimal propeller shape. We revisit the centerline optimization problem and now consider a swimmer with a spherical cargo of fixed radius, R, attached to leading end of the propeller. The swimmer shape over the course of an optimization with $\zeta = 50$ and $R/L = 0.12$ is shown in Supplementary Video 4. In the Stokes flow problem, the cargo is treated as a separate body a small distance away from the end of the propeller, but they are taken to move together as a connected rigid body. The hydrodynamic interactions between the cargo and the propeller are naturally accounted for through the boundary integral equations that we solve. The location of the cargo relative to the propeller can affect the swimming speed.[34] During the optimization, the propeller attachment point is allowed to move along the cargo's surface, and so in addition to the optimal propeller centerline shapes, there will also be an optimal location for the propeller attachment point to the payload.

We first use our approach to examine the swimmer geometry used in Ghosh and Fischer. We can generate a close approximation of this swimmer's shape by taking $L/R = 8.3$, $a/R = 0.52$, and a helical centerline (eq 3) with $\alpha = 0.65$ and k

dx.doi.org/10.1021/nl3040477 | Nano Lett. XXXX, XXX, XXX−XXX

= $4\pi/L$. The swimmer shape described by these parameters is shown in the top image of Figure 4. Using the boundary integral solver the nondimensional swimming speed, $V = \eta R^2 U_z/\tau_0$, is found to be $V^{GF} = 4.7 \times 10^{-4}$, while the nondimensional rotation rate, $W = \eta R^3 \Omega_0/\tau_0$, is $W^{GF} = 0.011$. Our gradient ascent method finds an optimal centerline geometry for a swimmer with $L/R = 8.3$ and $a/R = 0.52$. The result is the swimmer shape depicted in the bottom image of Figure 4. It has a speed of $V = 1.2 \times 10^{-3}$, more than 2.5 times greater than the original design.

$V^{GF} = 4.7 \times 10^{-4}$
$W^{GF} = 1.1 \times 10^{-2}$

$V_1^{OPT} = 1.2 \times 10^{-3}$
$W_1^{OPT} = 4.8 \times 10^{-3}$

$V_2^{OPT} = 2.2 \times 10^{-3}$
$W_2^{OPT} = 1.3 \times 10^{-2}$

Figure 4. A computational surface model that closely resembles that developed in Ghosh and Fischer[7] (top). For this swimmer, $L/R = 8.3$, $a/R = 0.52$, and the centerline is described by eq 3 with $\alpha = 0.65$ and $k = 4\pi/L$. The middle image shows a swimmer with the same values of a/R and L/R, but whose centerline has been optimized. The speeds of each of these swimmers is indicated, with the optimized swimmer having a higher speed by a factor of 2.55. Even higher speeds can be achieved if one considers different propeller lengths and aspect ratios as well as centerline shapes. The lower image shows a swimmer with $L/R = 5$ and $a/R = 0.2$. With this propeller shape, the swimming speed is increased by a factor of 4.68. The values of the nondimensional rotation rates, W, are also shown for each swimmer shape.

To understand this optimal shape, we perform a series of centerline optimizations for propeller cross-section radii $a/R = 0.2$ and $a/R = 0.4$ and propeller half-lengths $L \in [2R,8R]$ when $a/R = 0.2$ and $L \in [2R,10R]$ when $a/R = 0.4$. Figure 5 shows the optimal swimmer shapes over the range of L/R for the two values of a/R. The mobility coefficients for these shapes are given in the Supporting Information. While we again achieve optimal centerline shapes that resemble helices (see Figure 5), they are quite different from those found for propellers without a payload, even though the propeller aspect ratios are in the same range. Take, for example, the optimal swimmer with $\zeta = 30$ in Figure 2a and compare it to the corresponding case in Figure 5a where $a/R = 0.2$ and $L/R = 6$. Both propellers have the same value of ζ, but the centerline of the propeller with the attached cargo has fewer helical waves and a larger helical radius. These differences can be seen in detail by comparing the position data in Figures 2b and 5b. For the case $\zeta = 50$, a similar comparison can be made between the final $\zeta = 50$ shape in Figure 2a and the final shape shown in the Supplementary Video 4. We also note that, for a given propeller length, the optimizations with $a/R = 0.2$ and $a/R = 0.4$ yield very similar optimal shapes. We find, therefore, that the optimal swimmer shape does not depend strongly on the aspect ratio of the propeller but does on the size of the attached cargo. The optimal shape does vary with propeller length. The centerline position data (Figure 5b) show that both the number of helical waves and the helical radius of the optimal shape increase as the propeller gets longer. In addition to the propeller shape, we find that the location of the cargo relative to the propeller is important. For both choices of a/R, we see that, as the tail length increases, the location of the cargo's center moves toward the helical axis while the propeller attachment point moves to the side of the cargo.

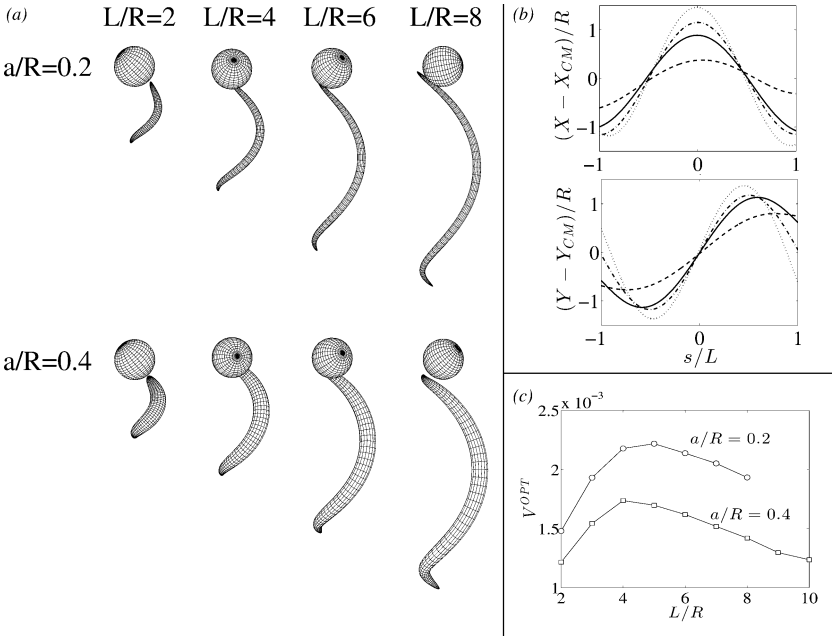

Figure 5. (a) Optimal shapes for swimmers with an attached cargo for different values of L/R and a/R. (b) The x and y components of $\mathbf{X}(s)$ as a function of s for the optimal shapes with $a/R = 0.2$ and normalized tail half-lengths $L/R = 2$ (dashed), 4 (solid), 6 (dash−dotted), and 8 (dotted). (c) The swimming speeds of the optimal shapes as a function of the normalized tail half-length. The line with the square markers shows the values when $a/R = 0.4$, while the line with the circular markers shows those for when $a/R = 0.2$.

dx.doi.org/10.1021/nl3040477 | Nano Lett. XXXX, XXX, XXX−XXX

The speed of the optimal shape also varies with the geometric parameters a/R and L/R. Figure 5c shows the nondimensional speed of the optimal shape as a function of L/R. For a given length, the values of the speed are higher for $a/R = 0.2$ where the propeller is thinner. Interestingly, for both cases of a/R, we find that the speed depends nonmonotonically on the propeller length. This indicates that, for cargo of a given size, there is an optimal propeller length. When $a/R = 0.4$, we find the optimal tail half-length to be $L \approx 4R$, while for $a/R = 0.2$, we see that it increases to $L \approx 5R$. Based on these results, the original Ghosh and Fischer design could be further improved by reducing the propeller length and increasing its aspect ratio. Such a swimmer is shown at the bottom of Figure 4, which gives a further increase in speed (assuming a fixed payload radius) of 468% over the original Ghosh and Fischer design. As a caveat, this optimized swimmer has a shorter, thinner propeller of decreased surface area and volume. Thus, it may take an applied magnetic field of much greater strength to obtain the same net applied magnetic torque upon the propeller to achieve its increased speed.

In this study, we utilized shape optimization and a boundary integral formulation of Stokes flow to identify several key design criteria for microswimmers and improvements to current microswimmer designs. The results that we have found are not only pertinent to the Zhang et al. and Ghosh and Fischer designs, but apply more generally and provide guidance in the design of new magnetic swimmers. We first demonstrated that when the cross-section of the propeller is elongated, its orientation matters. We showed that the long axis of the propeller cross-section should be perpendicular to the swimming direction. This orientation results in speeds approximately 70% greater than the aligned case. We then used shape optimization based on shape derivatives and a steepest ascent method to find the propeller centerline shapes that provide higher swimming speeds. We found that for swimmers *without* an attached payload, regardless of the propeller aspect ratio, a simple helical centerline with $\alpha = 0.84$ and $b/a = 2.2$ is nearly optimal. These optimal shapes, however, are drastically altered if there is a cargo attached to one end of the swimmer. Here, we found that it was advantageous to have the helical radius of the propeller similar to the radius of the attached cargo, and fewer helical waves than one might expect. We show such modifications to the original Ghosh and Fischer design, keeping the propeller of roughly the same surface area and volume, led to speeds 255% greater than the original value. By assuming that the same amount of magnetic torque could be applied on shorter, thinner propellers the increases could be yet larger. In addition, we find that the translation speed depends nonmonotonically on the tail half-length, with a maximum value being achieved when $L/R \approx 4-5$. In previous studies aimed at optimizing planar flagellum beating for spermatozoa,[24] a value $L/R = 12$ was reported for maximizing speed while keeping the viscous dissipation fixed. They found that this ratio was conserved across many species of sperm. It is interesting to note that the optimal ratio is of the same order as that found here despite profound differences in actuation mechanisms. Also, as with our optimizations, the wave shape differs substantially from the sawtooth pattern[22] that is found to be optimal when the sperm's head is ignored.

There are several interesting directions to explore further. First, in our optimization, we considered a rather general shape space for the centerline. Given very specific methods of micrometer-scale construction, such as the roll-up procedure used by Zhang et al.[8−10] or the glancing angle deposition methods by Ghosh and Fischer,[7] it would also be interesting to understand how geometric constraints associated with these construction techniques affect the optimal shapes. In this way, the effectiveness of one construction procedure over another could also be assessed. Still, it does appear that the deposition methods of Ghosh and Fischer could be easily adapted to investigate the optimized swimmers discussed here. In addition, our shape optimization algorithm could be used to maximize (or minimize) other quantities that are important to effective operation of these devices. These include optimization under conditions of an external flow, or where other forces, such as gravity, might be present. Also, considering these swimmers might be employed in suspension, it would be interesting to optimize swimmer geometries to control the flow fields they generate so as to suppress large-scale flow instabilities[35,36] that might arise from swimmer−swimmer hydrodynamic interactions.[37] In this study, we have identified design criteria based on hydrodynamic considerations and maximization of speed for a given torque. Our scheme could be modified to determine shapes that maximize the stroke efficiency or the distance traveled along the helical axis in one rotation. Indeed, the rotation rates and stroke efficiency values are different for the two optimal swimmers shown in Figure 4. It would be interesting to see how shapes maximized for stroke efficiency differed from those maximizing speed for a given torque. In addition, our algorithm could be modified to incorporate slip boundary conditions for the Stokes equations and determine how they might affect the optimal shape. In addition, our algorithm could be modified to incorporate slip boundary conditions for the Stokes equations and determine how they might affect the optimal shape. This would allow us to evaluate alternative propulsion mechanisms, such as those employed by chemically driven nanomotors and Janus particles,[38] where slip-layers are often present and used to drive swimmer motion. It would also be of interest to explore how the torque itself depends on the distribution of magnetic material within the body. This could also be done using the shape optimization techniques discussed here, through coupling it with Maxwell's equations. Finally, it is important to remember that our optimization techniques may well be finding only local maxima of our objective function (speed, under various constraints) and that other search methods or initial shapes could lead to yet faster devices.

■ ASSOCIATED CONTENT

Supporting Information

Videos of the optimizations shown in Figure 2a; video of an optimization with an attached pay-load PDF file containing descriptions of the optimization method, boundary integral equations, parametrization of swimmer surfaces, and the mobility coefficients of the optimal shapes. This material is available free of charge via the Internet at http://pubs.acs.org/.

■ AUTHOR INFORMATION

Corresponding Author

*E-mail: e.keaveny@imperial.ac.uk.

Notes

The authors declare no competing financial interest.

dx.doi.org/10.1021/nl3040477 | *Nano Lett.* XXXX, XXX, XXX−XXX

■ ACKNOWLEDGMENTS

We thank Jun Zhang for insightful discussions during this work. This work was supported by the Department of Energy grant FG02-88ER25053 and the National Science Foundation grants DMS-0700669 and DMS-0920930 and by its MRSEC program under DMR-0820341. S.W.W. also acknowledges support from the National Science Foundation grant DMS-1115636.

■ REFERENCES

(1) Bleil, S.; Marr, D.; Bechinger, C. *Appl. Phys. Lett.* **2006**, *88*, 263515.
(2) Biswal, S.; Gast, A. *Anal. Chem.* **2004**, *76*, 6448−6455.
(3) Rida, A.; Gijs, M. *Anal. Chem.* **2004**, *76*, 6239−6246.
(4) Doyle, P.; Bibette, J.; Bancaud, A.; Viovy, J.-L. *Science* **2002**, *295*, 2237.
(5) Dreyfus, R.; Baudry, J.; Roper, M. L.; Fermigier, M.; Stone, H.; Bibette, J. *Nature* **2005**, *437*, 862−865.
(6) Keaveny, E.; Maxey, M. *J. Fluid Mech.* **2008**, *598*, 293−319.
(7) Ghosh, A.; Fischer, P. *Nano Lett.* **2009**, *9*, 2243−2245.
(8) Zhang, L.; Abbott, J. J.; Dong, L.; Kratochvil, B. E.; Bell, D.; Nelson, B. J. *Appl. Phys. Lett.* **2009**, *94*, 064107.
(9) Zhang, L.; Abbott, J. J.; Dong, L. X.; Peyer, K. E.; Kratochvil, B. E.; Zhang, H. X.; Bergeles, C.; Nelson, B. J. *Nano Lett.* **2009**, *9*, 3663−3667.
(10) Zhang, L.; Peyer, K. E.; Nelson, B. J. *Lab Chip* **2010**, *10*, 2203−2215.
(11) Gao, W.; Kagan, D.; Pak, O. S.; Clawson, C.; Campuzano, S.; Chuluun-Erdene, E.; Shipton, E.; Fullerton, E. E.; Zhang, L.; Lauga, E.; Wang, J. *Small* **2012**, *8*, 460−467.
(12) Zerrouki, D.; Baudry, J.; Pine, D.; Chaikin, P.; Bibette, J. *Nature* **2008**, *455*, 380−382.
(13) Keaveny, E.; Shelley, M. *Phys. Rev. E* **2009**, *79*, 051405.
(14) Purcell, E. *Am. J. Phys.* **1977**, *45*, 3−11.
(15) Lauga, E.; Powers, T. R. *Rep. Prog. Phys.* **2009**, *72*, 096601.
(16) Nelson, B. J.; Kaliakatsos, I. K.; Abbott, J. J. *Annu. Rev. Biomed. Eng.* **2010**, *12*, 55−85.
(17) Abbott, J. J.; Peyer, K. E.; Lagomarsino, M. C.; Zhang, L.; Dong, L.; Kaliakatsos, I. K.; Nelson, B. J. *Int. J. Robotics Res.* **2009**, *28*, 1434−1447.
(18) Kim, S.; Karrila, S. J. *Microhydrodynamics: Principles and Selected Applications*; Dover Publications, Inc.: Mineola, NY, 2005.
(19) Mohammadi, B.; Pironneau, O. *Applied Shape Optimization for Fluids*; Numerical Mathematics and Scientific Computation; The Clarendon Press, Oxford University Press: New York, NY, 2001.
(20) Pironneau, O. *Optimal Shape Design for Elliptic Systems*; Springer Series in Computational Physics; Springer-Verlag: New York, NY, 1984.
(21) Pironneau, O.; Katz, D. F. *J. Fluid Mech.* **1974**, *66*, 391−415.
(22) Lighthill, J. *Mathematical Biofluiddynamics*; SIAM: Philadelphia, PA, 1975.
(23) Spagnolie, S. E.; Lauga, E. *Phys. Fluids* **2010**, *22*, 031901.
(24) Tam, D.; Hosoi, A. E. *Phys. Rev. E* **2011**, *83*, 045303.
(25) Wilkening, J.; Hosoi, A. E. *J. Fluid Mech.* **2008**, *601*, 25−61.
(26) Walker, S. W.; Shelley, M. J. *J. Comput. Phys.* **2010**, *229*, 1260−1291.
(27) Michelin, S.; Lauga, E. *Phys. Fluids* **2010**, *22*, 111901.
(28) Pozrikidis, C. *Boundary Integral and Singularity Methods for Linearized Viscous Flow*; Cambridge Texts in Applied Mathematics; Cambridge University Press, 1992; p 272.
(29) Keaveny, E. E.; Shelley, M. J. *J. Comput. Phys.* **2011**, *230*, 2141−2159.
(30) Drazer, G.; Koplik, J.; Acrivos, A.; Khusid, B. *Phys. Rev. Lett.* **2002**, *89*, 244501.
(31) Spagnolie, S. E.; Lauga, E. *J. Fluid Mech.* **2012**, *700*, 105−147.
(32) Lighthill, J. *SIAM Rev.* **1976**, *18*, 161−230.
(33) Tottori, S.; Zhang, L.; Qiu, F.; Krawczyk, K.; Franco-Obregón, A.; Nelson, B. J. *Adv. Mater.* **2012**, *24*, 811−816.
(34) Raz, O.; Leshansky, A. M. *Phys. Rev. E* **2008**, *77*, 055305.
(35) Hernandez-Ortiz, J.; Stoltz, C.; Graham, M. *Phys. Rev. Lett.* **2005**, *95*, 204501.
(36) (a) Saintillan, D.; Shelley, M. J. *Phys. Rev. Lett.* **2008**, *100*, 178103. (b) Saintillan, D.; Shelley, M. J. *Phys. Fluids* **2008**, *20*, 123304.
(37) Keaveny, E.; Maxey, M. *Phys. Rev. E* **2008**, *77*, 041910.
(38) Paxton, W.; Kistler, K.; Olmeda, C.; Sen, A.; St Angelo, S.; Cao, Y.; Mallouk, T.; Lammert, P.; Crespi, V. *J. Am. Chem. Soc.* **2004**, *126*, 13424−13431.

■ NOTE ADDED AFTER ASAP PUBLICATION

This Letter was published ASAP on January 22, 2013. Minor text changes have been made in the Abstract, Figure 1 caption, and text. The correct version was published on January 24, 2013.